How do Velocity Structure Functions Trace Gas Dynamics in Simulated Molecular Clouds?

R.-A. Chira[1], J. C. Ibáñez-Mejía[2,3], M.-M. Mac Low[4,5], and Th. Henning[1]

[1] Max-Planck-Institut für Astronomie, Königstuhl 17, 69117 Heidelberg, Germany
   e-mail: `roxana-adela.chira@alumni.uni-heidelberg.de`
[2] I. Physikalisches Institut, Universität zu Köln, Zülpicher Straße 77, 50937 Köln, Germany
   e-mail: `ibanez@ph1.uni-koeln.de`
[3] Max-Planck-Institut für Extraterrestrische Physik, Giessenbachstrasse 1, 85748 Garching, Germany
[4] Dept. of Astrophysics, American Museum of Natural History, 79th St. at Central Park West, New York, NY 10024, USA
   e-mail: `mordecai@amnh.org`
[5] Zentrum für Astronomie, Institut für Theoretische Astrophysik, Universität Heidelberg, Albert-Ueberle-Str. 2, 69120 Heidelberg, Germany

Abstract

Context. **Supersonic disordered flows accompany the formation and evolution of molecular clouds (MCs). It has been argued that this is turbulence that can support against gravitational collapse and promote the formation of hierarchical substructures. Yet, little is still known about what drives gas dynamics on MC scales.**

Aims. We investigate the time evolution of **gas dynamics** within simulated MCs. We focus on the following questions: What physical process dominantes the driving of **the disordered flows seen? How can these flows be characterized? Are they consistent with turbulence? Do the simulated flows agree with the observations?**

Methods. We follow the gas motions within three MCs that have formed self-consistently within kiloparsec-scale numerical simulations of the interstellar medium (ISM). The simulated ISM evolves under the influence of physical processes including self-gravity, magnetic fields, supernovae-driven turbulence, and radiative heating and cooling. **We characterize the flow using** velocity structure functions n(VSFs) and compare the obtained parameters with predicted **and observed** values.

Results. We demonstrate that the scaling exponent of VSFs and the self-similarity parameter are sensitive tools that trace the dominant driving sources of **the flow**. The trends are generally robust against the influence of projection, Jeans refinement level, and density-weighting. Yet, the detailed evolution may vary significantly depending on the density threshold.

Conclusions. We conclude that the VSF is a well placed and stable method for examining the composition, structure and evolution of turbulence within MCs. Yet, it is essential to clearly define the underlying conditions and assumptions of the analysis in order to clarify which part of the ISM is studied and to make the results comparable to analogue studies. In our case, we find clear indicators of how the VSF reacts to the dynamics in the simulated clouds: Gravitational contraction causes a flattening of the scaling exponent of the structure functions, but has no imprint on the self-similarity parameter of the structure function, unless the collapse is triggered by a shock. Nearby SN explosions inject turbulent energy on a wide range of scales onto MCs. This injection of energy is visible in in the structure functions and the self-similarity parameters, but only for a short period of time as the excess kinetic energy decays. **[comparison to observations?]**

Key words. keywords

1. Introduction

It has long been known that star formation preferentially occurs within molecular clouds. Yet **the star formation process is still not completely understood**. It is clear that gravity is the major factor as it drives collapse motions and operates on all scales. However, one needs additional processes that stabilise the gas **or terminate star formation quickly** in order to **explain low star formation efficiencies** observed in molecular clouds. Although there are many processes that act at the different scales of molecular clouds, **turbulent support has often been argued** to be the best candidate for this task.

In the literature, turbulence has an ambiguous role in the context of star formation. In most of the cases, turbulence is expected to stabilise molecular clouds on large scales (Fleck 1980; McKee & Zweibel 1992; Mac Low 2003), while feedback processes and shear motions heavily destabilise or even disrupt

cloud-like structures, offering a formation scenario for large filaments (Tan et al. 2013; Miyamoto et al. 2014). **[I don't really understand these cites to Tan & Miyamoto. Usually I contrast large scale support with small-scale compressive promotion of collapse.]** However, it remains unclear whether there are particular mechanisms that dominate the driving of turbulence within molecular clouds, **as every process is supposed to be traced by typical features in the observables. Yet, these features are either not seen or are too ambiguous to clearly reflect the dominant driving mode.** For example, turbulence that is driven by large-scale velocity dispersions during global collapse (Ballesteros-Paredes et al. 2011a,b; Hartmann et al. 2012) produces P-Cygni lines **that have not yet been observed on scales of entire molecular clouds**. Internal feedback, on the contrary, seems more promising as it drives turbulence outwards (Dekel & Krumholz 2013; Krumholz et al. 2014). Observations, though, demonstrate that the required driving sources need to act

on scales of entire clouds; which typical feedback, **such as radiation, winds, jets, or supernovae (SNe),** cannot achieve (Heyer & Brunt 2004; Brunt et al. 2009; Brunt & Heyer 2013).

There have been many theoretical studies that have examined the nature and origin of turbulence within the phases of the interstellar medium (ISM; Mac Low & Klessen 2004, and references within). The most established **characterization of turbulence in general was** by Kolmogorov (1941) who investigated fully developed, incompressible turbulence **driven on scales larger than the object of interest, and diffusing on scales much smaller than those of interest**. In the scope of this paper this object is a single molecular cloud. Molecular clouds are highly compressible, though. Only a few analytical studies have treated this case. She & Lévêque (1994) and Boldyrev (2002), for example, generalise and extend the predicted scaling of the decay of turbulence to supersonic turbulence. Galtier & Banerjee (2011) and Banerjee & Galtier (2013) provide an analytic description of the scaling of mass-weighted structure functions.

In this paper, we examine three molecular clouds that formed **self-consistently** from SN-driven turbulence in the simulations by Ibáñez-Mejía et al. (2016, 2017, Paper I and Paper II hereafter) and study how the turbulence within the clouds' gas evolves. The key questions we **address** are the following: What dominates the turbulence within the simulated molecular clouds? **How can structure functions inform us about the evolutionary state of MCs and the dominant physics processes within them?**

In Sect. 2, we introduce the simulated clouds in the context of the underlying physics involved in the simulations. Furthermore, we describe the theoretical basics of velocity structure functions. Sect. 3 demonstrates that the velocity structure function is a useful tool to characterise the dominant driving mechanisms of turbulence in molecular clouds and can be applied to both simulated and observed data. We also discuss the influences of utilising one-dimensional velocity measurements, different Jeans refinement levels, density thresholds and density weighting on the applicability of the velocity structure function and the results obtained with it in Sect. 4. We summarise our findings and conclusions in Sect. 5.

2. Methods

2.1. Cloud models

The analysis in this paper is based on a sample of three molecular clouds (MCs) found within a **three-dimensional (3D), magnetohydrodynamical, adaptive mesh refinement simulation using the FLASH code (Fryxell et al. 2000). Paper I and Paper II, as well as Chira et al. (2018, Paper III hereafter)**, describe the simulations and the clouds in more detail. We summarise the most relevant properties.

The numerical simulation models a $1 \times 1 \times 40$ **kpc**[3] section of the multi-phase, turbulent ISM of a disk galaxy, where dense structures form self-consistently in convergent, turbulent flows (Paper I). The model includes gravity—a background galactic-disk potential accounting for a stellar component and a dark matter halo, as well as self-gravity turned on after 250 Myr of simulated time—supernova-driven turbulence, photoelectric heating and radiative cooling, and magnetic fields. Although hundreds of dense clouds form within the simulated volume, Paper II focused on three clouds, which were re-simulated at a much higher spatial resolution, **which we map to a uniform grid of 0.1 pc zones.** In this paper, we use the data within $(40 \text{ pc})^3$ subregions centred in the high-resolution clouds' centres of mass. The in-

ternal structures of MCs are resolved using adaptive mesh refinement, focusing grid resolution on dense regions where Jeans unstable structures must be resolved with a minimum of 4 cells ($\lambda_J > 4 \Delta x_{\min}$). For a maximum resolution of $\Delta x = 0.1$ pc, the corresponding maximum resolved density is 8×10^3 cm^{-3} for gas at a temperature of 10 K (e.g. Paper II, Eq. 15). This means that we can trace fragmentation down to 0.4 pc, but cannot fully resolve objects that form at smaller scales. The MCs have initial masses at the onset of self-gravity of 3×10^3, 4×10^3, and 8×10^3 M$_\odot$ and are denoted as M3, M4, and M8, respectively, hereafter.

However, it is important to point out that the clouds are embedded within a complex turbulent environment, gaining and losing mass as they evolve. **Paper II described the time evolution of the properties of all three clouds in detail, in particular, mass, size, velocity dispersion, and accretion rates, in the context of MC formation and evolution within a galactic environment.** Paper III studied the properties, evolution, and fragmentation of filaments that self-consistently condense within these clouds. They paid particular attention to the accuracy of typical stability criteria for filaments, comparing their measurements to the theoretical predictions, showing that theoretical models do not capture the complexity of fragmentation due to their simplifying assumptions.

In this paper, we focus on the driving sources of turbulence within the simulated MCs and the signatures they imprint on **the velocity structure function (VSF)**.

2.2. Velocity Structure Function

We probe the power distribution of turbulence throughout the entire simulated MCs by using the VSF. The VSF is a two-point correlation function,

$$S_p(\ell) = \langle |\Delta \mathbf{v}|^p \rangle \tag{1}$$

that measures the mean velocity difference to the pth power

$$\Delta \mathbf{v}(\boldsymbol{\ell}) = \mathbf{v}(\mathbf{x} + \boldsymbol{\ell}) - \mathbf{v}(\mathbf{x}) \tag{2}$$

between two points $\mathbf{x}$ and $\mathbf{x} + \boldsymbol{\ell}$, with $\boldsymbol{\ell}$ being the direction vector pointing from the first to the second point. S_p **is usually reported as a function of** lag distance, $\ell = |\boldsymbol{\ell}|$, between the correlated points. The VSF estimates the occurrence of symmetric motions (e.g., rotation, collapse, outflows), as well as rare events in random turbulent flows (e.g., supernovae) in velocity patterns. Those patterns become more prominent the higher the value of p (Heyer & Brunt 2004). **Padoan et al. (2016) defined a density-weighted velocity structure function**

$$S_p(\ell) = \frac{\langle \rho(\mathbf{x})\rho(\mathbf{x} + \boldsymbol{\ell}) |\Delta \mathbf{v}|^p \rangle}{\langle \rho(\mathbf{x})\rho(\mathbf{x} + \boldsymbol{\ell}) \rangle}. \tag{3}$$

In many cases, though, a three-dimensional computation of the VSF cannot be performed because of the observational constraint that only line-of-sight velocities are available. We will therefore compare our three-dimensional (3D) results to one-dimensional (1D), density-weighted VSFs

$$S_{p,1D}^d(\ell) = \frac{\langle \rho(\mathbf{x})\rho(\mathbf{x} + \boldsymbol{\ell}) |\Delta \mathbf{v} \cdot \mathbf{e}_i|^p \rangle}{\langle \rho(\mathbf{x})\rho(\mathbf{x} + \boldsymbol{\ell}) \rangle}, \tag{4}$$

with $\mathbf{e}_i$ representing the unit vector along the $i = x$-, y-, or z-axis.

The first several orders of the VSF have a physical meaning. For example, S_1 **gives the mean of relative velocities between any two points** reflecting the modes created by different

gas flows, while S_2 is proportional to the kinetic energy, making it a good probe of how the turbulent energy is **distributed among** different scales.

For fully developed turbulence the VSF is well-described by a power-law relation (Kolmogorov 1941; She & Lévêque 1994; Boldyrev 2002):

$$S_p(\ell) \propto \ell^{\zeta(p)}. \qquad (5)$$

Note that the scaling exponent of that power-law relation, ζ, depends on many parameters, such as the order of the VSF, as well as the properties and composition of the studied turbulent flow, such as its geometry, compressibility, or magnetization. Many studies of VSFs distinguish between longitudinal and transverse velocity components, or compressible and solenoidal components, because those are expected to behave differently, especially towards larger lag distances (Gotoh et al. 2002; Schmidt et al. 2008; Benzi et al. 2010). However, the differences are mostly negligible on the scales we focus on. **Since these decompositions are also hard to perform on observational data, we focus only on the total VSF.**

Theoretical studies predict values of ζ depending on the nature of the turbulence and the order p. For example, Kolmogorov (1941) predicts that the third-order exponent, $\zeta(3)$, is equal to unity for an **incompressible flow**. This results in the commonly known prediction that the kinetic energy decays with $E_{\mathrm{kin}}(k) \propto k^{-\frac{5}{3}}$, with $k = \frac{2\pi}{\ell}$ being the wavenumber of the turbulence mode.

For a supersonic flow, however, $\zeta(3) > 1$ **is expected.** Based on Kolmogorov's work, She & Lévêque (1994) and Boldyrev (2002) extended and generalised the analysis and predicted the following. For an incompressible filamentary flow She & Lévêque (1994) predict that the VSFs scale with **power law index**

$$\zeta(p) = \frac{p}{9} + 2\left[1 - \left(\frac{2}{3}\right)^{\frac{p}{3}}\right], \qquad (6)$$

while supersonic flows with sheet-like geometry are **predicted** to scale with (Boldyrev 2002)

$$\zeta(p) = \frac{p}{9} + 1 - \left(\frac{1}{3}\right)^{\frac{p}{3}}. \qquad (7)$$

Benzi et al. (1993) introduced the principle of extended self-similarity. It proposes that there is a constant relationship between the scaling exponents of different orders at all lag scales **so that ζ can be measured from S_p^d / S_3^d, which typically gives much clearer power-law behavior. The self-similarity parameter is defined as,**

$$Z(p) = \frac{\zeta(p)}{\zeta(3)}. \qquad (8)$$

Since **the predicted values for $\zeta(p)$ by She & Lévêque (1994) and Boldyrev (2002)** are normalised so that $\zeta(3) = 1$, Eq. (6) and (7) also provide the predictions for $Z(p)$, respectively.

For the discussion below, we measure ζ by fitting a power-law, given by

$$\log_{10}\left[S_p^d(\ell)\right] = \log_{10}(A) + \zeta \log_{10}(\ell), \qquad (9)$$

with A being the proportionality factor of the power-law to the simulated measurements.

In order to reduce the computational effort, we divide the range of 3D lag distances, $|\boldsymbol{\ell}|$, into 40 equidistantly separated bins ranging from 0.1 to 30 pc. **[there must be more to your optimization method than this. Fill in the details?]** This means that the measurements at the given lag interval ℓ_i we will show below are based on data with lag distances $\ell_{i-1} < \ell \le \ell_i$.

[I have moved all the methodological material from Sections 3 and 4 back into this section]. For our calculations, **we focus on clouds, defined as regions above a fixed number density threshold with fiducial value $n_{cloud} = 100$ cm^{-3}. We have chosen this threshold as it roughly corresponds to the density when CO becomes detectable.** However, Paper II shows that there is usually no sharp increase in density between the ISM and the clouds. Instead, the gas becomes continuously denser towards the centres of mass within the clouds. Consequently, **our use of** a density threshold is a **somewhat artificial boundary** between the clouds and the ISM. Observationally, however, introducing a **column** density (or intensity) threshold is unavoidable, be it due to technical limitations (e.g., **detector sensitivity**) or the nature of the underlying physical processes (for example, excitation rates, or critical densities). Therefore, it is important to study **how a density threshold influences the VSF and its evolution.**

At our fiducial density threshold, we actually consider only $\le 1.5\%$ of the volume in the high resolution cube. Removing the density threshold, by setting $n_{cloud} = 0$ cm^{-3}, results in analysing the entire data cube. As this would be too computationally expensive, **when we study this case** we randomly choose a set of 5% of the total number of cells as reference points and compute relative velocities to these cells only. We emphasise that this does not mean that we only calculate the relative velocities between these cells. Rather this subsample of cells represent the starting vectors $\boldsymbol{x}$ to which the velocities of all other cells $\boldsymbol{x} + \boldsymbol{\ell}$ in the same cube are compared to. This way we reduce the risk of ignoring or emphasising any spatial direction or angle.

Note that by choosing the starting points randomly we ensure that all parts of the cubes are considered. As a consequence, there is only a small likelihood (5% × 1.5% = 0.075%) that **any given cell chosen will be in the cloud.** Therefore, we emphasise that it is likely that the two subsamples (no density threshold and cloud-only) do not **have a common subset of starting vectors. Nevertheless, the random sample still includes $> 4 \times 10^3$ cells in the cloud, so the sample does include information on VSFs of material in the cloud.**

3. Results

In this section, we present our results on how velocity structure functions (VSFs) reflect the distribution of turbulent power within molecular clouds.

3.1. Examples

Fig. 1 shows three examples of VSFs, (a) cloud M4 at $t = 1.2$ Myr after self-gravity has been activated in the simulations, (b) M3 at $t = 3.5$ Myr, and (c) M3 at $t = 4.0$ Myr. All plots show the **density-weighted** VSFs of orders $p = 1$–3. The solid lines show the fitted power-law relations as given in Eq. (9).

The examples demonstrate that, in general, the measured VSFs cannot be described by a single power-law relation over the entire range of ℓ. Instead they are composed of roughly three different regimes: one at small scales at $\ell \lesssim 3$ pc, a second one within 3 pc $\lesssim \ell \lesssim$ 10–15 pc, and the last one at large scales with $\ell > 15$ pc. **We find that** only the small and intermediate ranges may be represented by a common power-law relation. On larger scales, one observes a local minimum before the VSFs either increase or stagnate. The location of the minimum coincides with
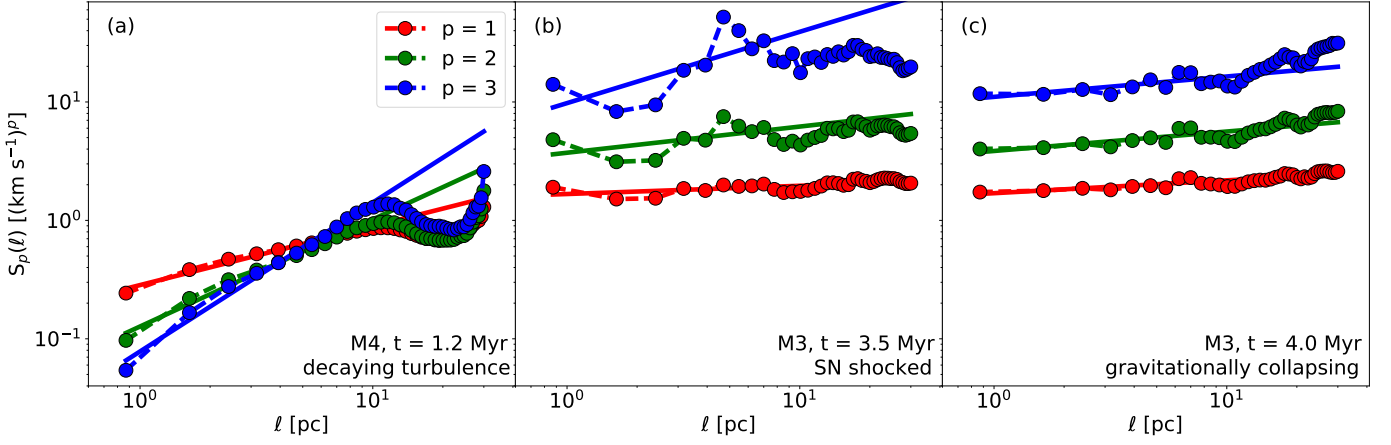
Figure 1: Examples of velocity structure functions as function of the lag scale ℓ and order p. The dots (connected by dashed lines) show the values computed from the simulation. The solid lines represent the power-law relations fitted to the respective structure functions.

the equivalent radius of the cloud, the radius a cloud of given mass would have if it would be a sphere. **[this is a pretty big claim to make based on one example. Can you make a plot showing the minimum location vs the equivalent radius for all three clouds for several times? Otherwise, I'd consider cutting it.]** Thus, in this context the VSF is an accurate tool to measure the size of a molecular cloud. On smaller scales, which correspond to individual clumps and cores, one sees significant differences.

The examples in Fig. 1 illustrate how VSFs react to different scenarios that affect the turbulent structure of the entire clouds. **Fig. 1(a) shows the case where turbulence is driven on large scales and naturally decays towards smaller scales. This is the most common behavior seen in all three MCs within the first ~1.5 Myr of the simulations.** During this interval of time the clouds experience the effect of self-gravity for the first time in their evolution and need to adjust to this new condition. Until this is the case, their VSFs are dominated by the freely cascading turbulence that previously dominated the kinetic structure of the clouds. Furthermore, this implies that we can only reliably examine turbulence within the simulations after 1.5 Myr and carefully need to take this into account in the further discussion (see Ibáñez-Mejía et al. 2017; Seifried et al. 2017).

The other examples represent the clouds at later stages of their evolution when the VSFs are dominated by sources that drive the **flow** within the clouds in a more extreme way. Fig. 1(b) shows the VSF of `M3` at a time when the cloud has just been hit by a SN shock front. One clearly sees how the amplitude of the VSFs is increased by one to two orders of magnitudes compared to the previous example. Especially the power **at small scales ($\ell \lesssim$ few parsecs) is highly amplified** as a result of the shock, **while it also reduces** the equivalent radius of the cloud. **[is that first minimum the thickness of the post-shock region, or the equivalent radius of the cloud? I'd bet that it's the former.]** Despite the increase of turbulent power at small scales, a large amount of energy is injected at large scales, as well. All this results in a **shallower slope of the VSF.** However, the effect of SN shocks last for only a short period of time (see below).

The last example, Fig. 1(c), demonstrates the imprint of gravitational contraction. Here, the VSF is almost flat, or even slightly increasing towards smaller separation scales. This kind of profile is typical for gas that is self-gravitationally contracting

(Boneberg et al. 2015; Burkhart et al. 2015) since gas moves into the inner regions of the cloud, reducing the average lag distances, but not necessarily the relative velocities. The latter may even be accelerated by the infall. As a consequence, large amounts of kinetic energy are transferred to smaller scales which flattens the corresponding VSF.

3.2. Time Evolution

Fig. 2(a) plots the time evolution of the power-law index $\zeta(p)$ fit to the VSF obtained for each cloud, and each order p . The figure shows several interesting features. First, initially, at $t = 0$ Myr, all calculated values of ζ are above the predicted values (see Eqs. (6) and (7)). **[can you indicate this on the figure?]** **This suggests that we are seeing excess power at large scales from the initial convergent flows that formed the clouds.** Second, ζ for all orders decreases with time as the clouds gravitationally collapse. **Distributed gravitational collapse causes an increase in relative velocities at increasingly small scales as material falls into filaments and nodes. The increase in small-scale power leads to a flattening of the VSF and thus a decrease in ζ.** Third, occasionally one observes bumps and dips in all orders of VSFs (e.g., `M3` or `M8` around $t = 1.7$ Myr). These features only last for short periods of time (up to 0.6 Myr), but set in **rather abruptly and represent sudden changes in large-scale power that change the VSF slope.**

[para out of place?] `M8` seems to develop differently. At the time the SN occurring at $t = 0.8$ Myr hits the cloud the values of ζ do not rise, as they have done within the other two clouds, but instead they drop. After the shock all scaling exponents grow to levels that are slightly above the pre-shock values, before they slowly decrease again.

Fig. 3(a) shows the time evolution of the self-similarity parameter, Z. One sees that most of the time the measured values of Z are in agreement or at least closely approaching the predicted values. **The occasional peaks in Z (for example, in `M4` at $t = 4.1$ Myr) occur at times when the scaling exponents of the VSFs $\zeta(3)$ reach values close to or below 0.** The decreases in Z (for example, in `M3` around $t = 1.8$ Myr), on the other hand, occur when SN shocks hit and heavily impact the clouds, **producing stronger effects in higher order VSFs.**
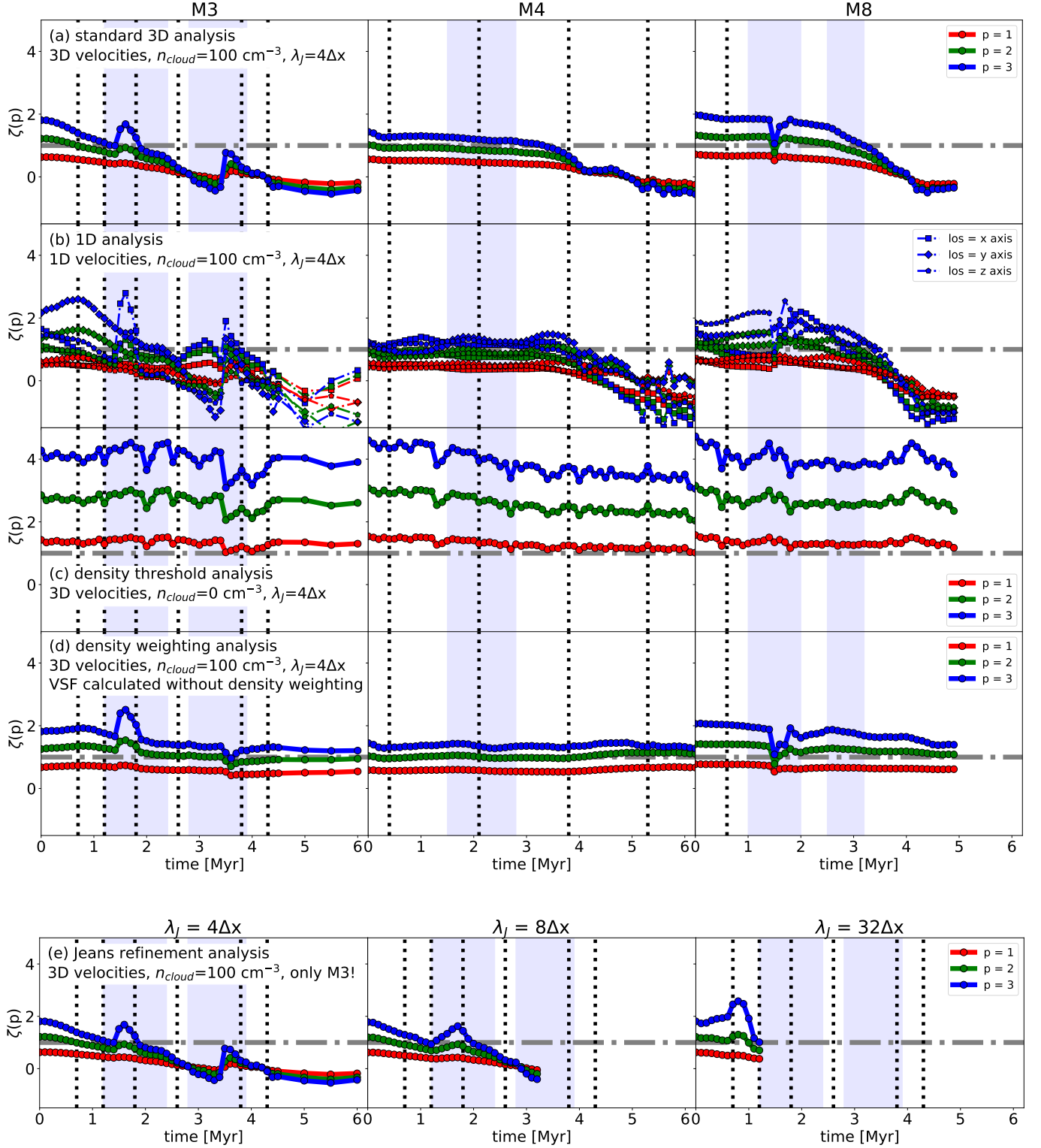
Figure 2: Time evolution of scaling exponent $\zeta(p)$ of the pth order VSF. Panels (a)–(d) show the measurements for M3 (*left*), M4 (*middle*), and M8 (*right*), respectively. Of these, (a) represents the standard analysis while the other rows illustrate the results of **different variations in the analysis as noted in the figures.** Panel (e) shows the values of ζ measured within M3 as a function of the Jeans refinement level the cloud has been modelled with. **Note that these more expensive runs were not run for as long as the fiducial run. In all panels, the grey dotted vertical lines mark the times than a SN explodes in the vicinity of the corresponding cloud, while the blue areas indicate periods of enhanced mass accretion onto the clouds. [What is the horizontal, grey, dot-dash line?]**
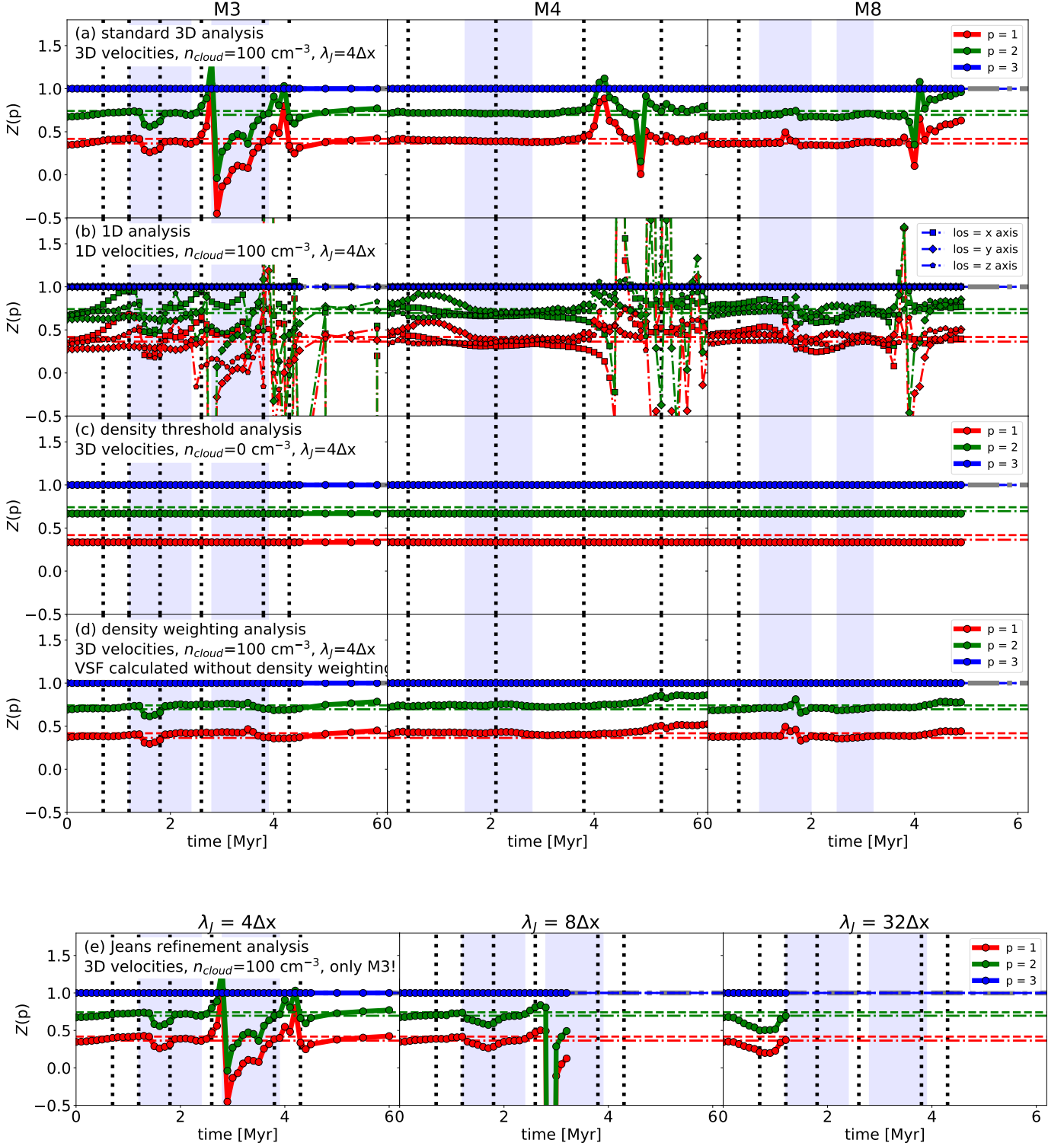
Figure 3: Like Fig. 2, but for the measured self-similarity parameter $Z = \zeta(p)/\zeta(3)$ of the pth order VSF. The coloured horizontal lines show the predicted values for incompressible turbulence (dash-dotted lines She & Lévêque 1994) and **for highly compressible, supersonic turbulence (dashed lines; Boldyrev 2002).**

In the rest of this section, we study how VSFs **computed in different ways compare to these density weighted results.** We compare the findings with the results we have obtained with our original setup. In Sect. 4, we will discuss and interpret these results in more detail.

3.3. Line-of-Sight VSF

Previously, we have seen how the VSF behaves and evolves within the clouds. By doing so, we derived the relative velocities based on the 3D velocity vectors **from the simulations. However, observed VSFs can only be measured using line-of-sight velocities.** Thus, in this subsection we investigate how VSFs derived from 1D relative velocities compare to the 3D VSFs presented before.

Figures 2(b) and 3(b) show measured ζ and Z, respectively, derived based on Eq. (4). We see that, in most of the cases, all 1D VSFs agree well with each other, as well as with the corresponding 3D VSFs. Yet, there are cases in which the 1D VSF evolves temporarily or completely differently than the 3D VSF. For example, the 1D VSF along the x-axis in `M3` initially behaves like the corresponding 3D VSF, though with lower absolute values of ζ (or higher values of Z). However, during the period $t = 2.5$–3.8 Myr the functions diverge. While the 3D ζ **decreases** further and switches sign, the ζ based on the 1D VSF along the x-axis shows a local maximum before converging with the 3D ζ again.

3.4. Density Thresholds

We now examine the VSFs of the entire data cubes without setting a density threshold ($n_{\mathrm{cloud}} = 0$ cm^{-3}). Figure 2(c) shows ζ, while Figure 3(c) shows Z in this case. These Figures clearly illustrate that the measurements in the samples without density threshold completely differ from those with the density threshold. Fig. 2(c) shows that the measured values of ζ are much higher in the ISM than in the cloud-only sample. Although we see a similar decline of ζ in `M4` and `M8` as the gas contracts under the influence of gravity in the vicinity of the clouds, ζ generally evolves differently here than **in the analysis focused on the clouds.** We see a high rate of random fluctuations in the evolution of ζ, as well. Furthermore, contrary to all of our other test scenarios, we see here that all Z are constant in time and within all clouds, with values slightly lower than those predicted by She & Lévêque (1994) for **incompressible** flows. **This is consistent with the high sound speed in the hot gas that fills most of the volume of the computational box, which results in subsonic flows predominating.**

3.5. Density Weighting

As mentioned in Sect. 2.2, Eq. (1) represents the definition of the density-weighted VSF. **While this represents the observational situation better, the theoretical predictions were developed for the unweighted statistic. Thus a comparison of results for the two variations in our model is of interest.** There are a few studies that have targeted this question (e.g., Benzi et al. 1993; Schmidt et al. 2008; Benzi et al. 2010; Gotoh et al. 2002). However, all of them considered **isotropic, homogeneous, turbulent flows** that are not comparable to our clouds. Padoan et al. (2016) use both methods, but not on the same set of data.

In this section, we investigate the influence of density weighting on VSFs by repeating the original analysis with the non-weighted VSF given by Eq. 1. Figs. 2(d) and 3(d) show the measured values of ζ and Z derived from the non-weighted VSFs, respectively.

Comparing the weighted and non-weighted samples, we see the following: The non-weighted ζ (Fig. 2d) traces the interactions between the gas of the clouds and the SN shocks in the same way as occurs for the density-weighted VSF. In `M3` and `M8`

we also see that the values of ζ decrease as the clouds evolve, yet not as fast as they do in the density-weighted VSFs. The measurements in `M4`, however, are almost constant over time. In all the cases, the values of ζ never **decrease** below 0.5; a behaviour that clearly differs from what we have observed in the density-weighted VSFs. **[somewhere we need to explain that this means that taking out the density weighting decreases the effective small-scale power, explaining the higher values of zeta. Maybe this is done below.]**

We observe a similar behaviour for measured values of Z (**Fig 3d**). **The density weighting weakens the influence of the highly compressible flows in the densest regions, but not so much as in the case with no density threshold. As a result the values of Z fluctuate slightly when shocks hit, and otherwise vary between the compressible and incompressible limits.** However, the evolution of Zs is smoother as there is no sign inversion of ζ. This means that we do not have any strong peaks in Z indicating the time when $\zeta(3)$ approaches 0, which happened when the majority of the turbulent power has transferred to the small scales. **[this needs to be mentioned in the initial analysis.]**

[move to 4, after discussion of Jeans length refinement?] Fig. 4 summarises the comparison of ζ (*top*) and Z (*bottom*) measured with the density-weighted (*abscissas*) and non-weighted VSFs (*ordinates*) for all Jeans refinement levels (**meaning the granularity used for modelling the turbulent motions of the gas, see Sect. 3.6 for more details**). The figure clearly shows that the measurements only agree well for the highest refinement level with $\lambda = 32\Delta x$. However, we would need more data point to be sure that this correlation is indeed real. At lower refinement level the measurements, **as those used for the standard analysis and all other test scenarios but the one presented in Sect. 3.6,** correlate less well with each other. The differences in the samples appear dominantly when the density-weighted ζ cease below ≈ 0.5, which is the global minimum for the non-weighted ζ. This means that none of the ζ computed in all clouds and refinement levels with the non-weighted VSF is measured to be below 0.5.

3.6. Jeans Length Refinement

The results we have discussed so far are based on simulation data presented in Paper I and Paper II. Due to the huge computational expense of the variety of physical and numerical processes (fluid dynamics, adaptive mesh refinement, supernovae, magnetic fields, radiative heating and cooling, and many more) within those simulations, though, they have required some compromises. One of these compromises was the Jeans refinement criterion used as part of the AMR mechanisms. The authors resolved local Jeans lengths by only four cells ($\lambda_J = 4\Delta x$). This is the minimal requirement for modelling self-gravitating gas in disks in order to avoid artificial fragmentation (Truelove et al. 1998). Other studies, for example by Turk et al. (2012), have shown that a significantly higher refinement is needed to reliably resolve turbulent structures and flows within disks to resolve turbulence. In our case, the key question is how quickly the turbulent cascade fills in after the multiple steps of refinement to higher resolution required to develop the high resolution cubes we use. Although we have a different physical situation, the earlier results still emphasize the importance of how well the Jeans length is resolved.

In the appendix of Paper II, the authors examine the effect the number of cells used for the Jeans refinement has on the
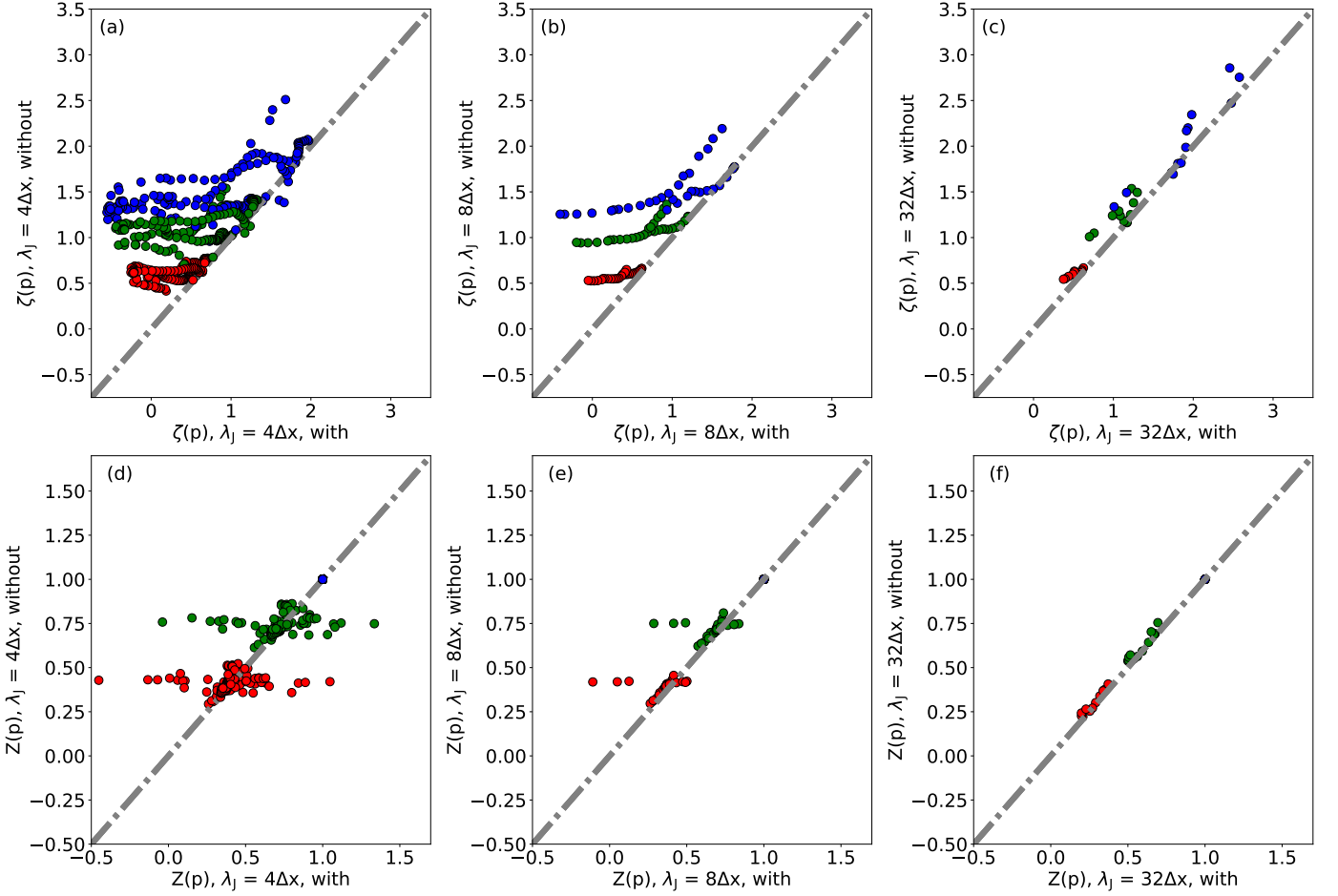
Figure 4: Comparison of ζ (*top*) and Z (*bottom*) measured based on density-weighted VSFs (*abscissas*) and non-weighted VSFs (*ordinates*).

measured kinetic energy. For this, they have rerun the simulations of M3 twice; once with $\lambda_J = 8\Delta x$ for the first 3 Myr after self-gravity was activated, and once with $\lambda_J = 32\Delta x$ for the first megayear of the cloud's evolution. The authors show that the $\lambda_J = 32\Delta x$ simulations smoothly **recover** the energy power spectrum on all scales already after this first megayear. The other two setups do this, as well, **but only over longer timescales.** This is why one can only reliably trust the findings in this paper after the clouds have evolved for approximately 1.5 Myr (see also Ibáñez-Mejía et al. 2017; Seifried et al. 2017).

Furthermore, Paper II calculated the difference in the cloud's total kinetic energy as a function of time and refinement level. They found that the $\lambda_J = 4\Delta x$ simulations miss a significant amount of kinetic energy, namely up to 13% compared to $\lambda_J = 8\Delta x$ and 33% compared to $\lambda_J = 32\Delta x$. However, they also observed that these differences peak around $t = 0.5$ Myr and decrease afterwards, as the $\lambda_J = 4\Delta x$ and $\lambda_J = 8\Delta x$ simulations adjust to the new refinement levels. Thus, the results we have derived from the $\lambda_J = 4\Delta x$ simulations need to be evaluated with respect to this lack of turbulent energy, although the clouds' dynamics remains dominated by gravitational collapse. It also means that the $\lambda_J = 4\Delta x$ data become more reliable the longer the simulations evolve.

In order to study how the level of Jeans refinement influences the behaviour of the VSFs, we investigate the M3 data of the $\lambda_J = 8\Delta x$ and $\lambda_J = 32\Delta x$ simulations. Figs. 2e and 3e show ζ and Z

for $\lambda_J = 8\Delta x$ and $\lambda_J = 32\Delta x$. In Fig. 5 we directly compare the measurements of all refinement levels relative to $\lambda_J = 4\Delta x$.

$\lambda_J = 8\Delta x$ shows the same behaviour as $\lambda_J = 4\Delta x$, with values in both samples being in good agreement as the top panel of Fig. 5 demonstrates. Over the entire observed time span, the measured values of ζ decrease as the VSF become flatter. At the time the SNe interact with the cloud, **over the course of about a megayear after traveling across the distance from the point of explosion to the cloud, the VSFs steeply increase toward larger scales causing values of ζ (Fig. 2e) to jump. [but this seems to contradict Fig1 that shows shallower slopes after impact by SNe]**, Compared to the $\lambda_J = 4\Delta x$ sample, the peak in ζ is smoother and lasts longer **at higher Jeans resolution**.

These same effects can be seen in Fig. 3e where the drop of Z due to the SN shock lasts longer than it did for $\lambda_J = 4\Delta x$. Besides this, the time evolution of Z for $\lambda_J = 8\Delta x$ is as sensitive to the turbulence-related events as it was for $\lambda_J = 4\Delta x$. The divergence produced when gravity has transferred the majority of power to smaller scales occurs at the same time. **The actual depth of the drop is a numerical artefact caused by $\zeta(3)$ being equal or close to zero at this very time step.**

The picture changes when we analyse the VSFs based on the $\lambda_J = 32\Delta x$ runs (Figs. 2e, 3e, and 5). Here one sees that the measured values of both ζ (Fig. 2e) and Z (Fig. 3e) are similar to those for $\lambda_J = 4\Delta x$ for the first 0.2 Myr. After this short period, though, the evolution of ζ diverge. While $\zeta(1)$ and $\zeta(2)$ continue to decrease **similar to $\lambda_J = 4\Delta x$ but at lower rate,** $\zeta(3)$ in-

creases until it peaks at $t = 0.8$ Myr and falls steeply again. This divergence has notable impact on the evolution of Z, as well. The bottom panel of Fig. 5 illustrates the different evolutions of measured ζ and Z in the two simulations more clearly. One sees that the differences between the samples follow the same pattern for all orders of p. The differences, though, increase with the order: While the values for $\zeta(1)$ are still in good agreement, the measured values of $\zeta(2)$ and $\zeta(3)$ for $\lambda_J = 32\Delta x$ are 40% and 100% higher than those measured for $\lambda_J = 4\Delta x$, respectively. Consequently, this causes differences in $Z(p)$ of 30–52% between the simulations. At $t = 1.2$ Myr, the last time step of this sample, the values of all ζ equal the measurements of $\lambda_J = 4\Delta x$ again. **As the cost of extending the $\lambda_J = 32\Delta x$ simulation is prohibitive, we cannot determine whether this agreement will continue.**

4. Discussion

[This is new text trying to recast the existing discussion]. We have seen in Sect. 3 that density-weighted VSFs reflect a combination of uniform, compressible turbulence, large-scale shocks, and gravitational collapse. Extended self-similarity emphasizes the turbulent nature of these high-Reynolds numbers flows even in regions of gravitational collapse.

As the clouds gravitationally collapse, the resulting increase in small-scale power flattens or even inverts the density-weighted VSFs, resulting in decreasing or even negative values of ζ (Fig. 2(a)). The increase in small-scale power can also be derived from the increasingly negative binding energy of the clouds as further gas falls into them (Paper II). Extended self-similarity shows VSF ratios characteristic of compressible turbulence (Fig. 3a), as can be seen from their tending to lie between the incompressible limit of She & Lévêque (1994) and the extremely compressible Burgers turbulence limit of Boldyrev (2002). The extended self-similarity procedure fails as $\zeta(3)$ passes through zero, however, so it must be interpreted in concert with the raw values of ζ.

The impact of SN shocks hitting the clouds is to inject power at all scales (Fig. 1). The resulting VSFs tend to lose their power-law character. Fitting a power-law to them anyway results in substantial perturbations from the predictions for compressible turbulence even under extended self-similarity. Fig. 3 shows times of SN explosions and periods of strong accretion onto the clouds. Note that the SN shock fronts move at speeds of 50–100 km s^{-1} through the ISM and the explosions occur at distances of 30–100 pc from the clouds, so the shocks need around 1 Myr to reach the clouds. Perturbations in Z not associated with zero-crossings by $\zeta(3)$ are consistent with being caused by SN shock front interactions with the clouds. These shock interactions last for only a fraction of a megayear, though, after which the turbulent nature of the flow reasserts itself.

4.1. Line-of-Sight Velocities

Our discussion so far has focused on 3D measurements of VSFs (Eq. [1]). In Sect. 3.3 we have seen that the ζ and Z derived from the 1D VSFs generally evolve similarly as those derived from the 3D VSFs. Yet, we have also seen that individual sight lines may evolve differently. These differences appear to reflect the detailed geometry of shock impacts on the cloud, which are reflected more strongly in the higher-order VSFs. For example, for the first 2 Myr of the evolution of M4 the values of Z along the y-axis are significantly higher

than those observed along the other axes and diverge significantly from the values expected for uniform turbulence. Recall that a perturbation in Z usually corresponds to an episode of strong shock driving, suggesting an impact along the y-axis at this time. Along the other two axes, Z continues to agree with supersonic turbulence (Boldyrev 2002). Note that this effect is only visible as we analyse the three dimensions separately, while the driving of the gas along the y-axis is averaged out in the 3D VSFs (see Fig. 3a).

In summary, **for a fully developed 3D turbulent field we expect that 1D VSFs behave similarly to 3D VSFs.** However, when there is a preferred direction along which the gas flows, the 1D and 3D VSFs differ significantly from each other. Thus, we predict that observed VSFs reflect the nature of turbulence within molecular clouds unless there is clear evidence that the gas is driven in a particular direction (e.g., by **a stellar wind** or SN shock front).

Note that this analysis does not take typical line-of-sight effects, such as optical depth or blending, into account. **Future studies need to investigate this point in more detail by performing VSF analyses based on full radiative transfer calculations.**

4.2. Density Thresholds

We find that the structure and behaviour of VSFs strongly depends on whether or not we assume a density threshold in computing them. In the fiducial case, where $n_{cloud} = 100$ cm^{-3}, we have seen a mostly straight decline of ζ while Z remains fairly constant over time, reflecting the contraction of the clouds due to self-gravity. **On the other hand, if we remove the density threshold, including the entire high-resolution region in the calculation, we observe a completely different picture. The high velocities present in the diffuse interstellar medium surrounding the cloud lead to strong large-scale power and thus much steeper VSFs, corresponding to higher values of ζ.** There is still a slightly declining trend in ζ, but the evolution is dominated by random fluctuations. We also see that Z **remains constant for the entire simulation in every case. The VSFs for the entire box appear consistent with the prediction for the value in incompressible turbulence (Boldyrev 2002). This suggests that they are dominated by the subsonic flow in the hot gas with $T > 10^6$ K that occupies most of the volume of the box.**

We conclude that the decision of whether or not a density threshold is used **has a significant and direct influence on the resulting VSFs. Indeed,** it is a straight-forward approach to **focus the analysis** on the actual area of interest. In observational studies such a threshold will anyway always be present as minimal collision rates for excitation or the sensitivity of detectors automatically introduce implicit density or intensity thresholds. Although we have only tested two specific setups in this context we have seen the significance of a proper choice of the density threshold, as well as a proper discussion of the obtained results considering the threshold as one of the defining parameters.

4.3. Density Weighting

In this subsection, we discuss the effect **of computing the VSF with or without including density weighting, relying on the results presented in Sect. 3.5. As long as the turbulence is dominated by the large scales, and a density threshold is used,** considering the density weighting does not have a signif-
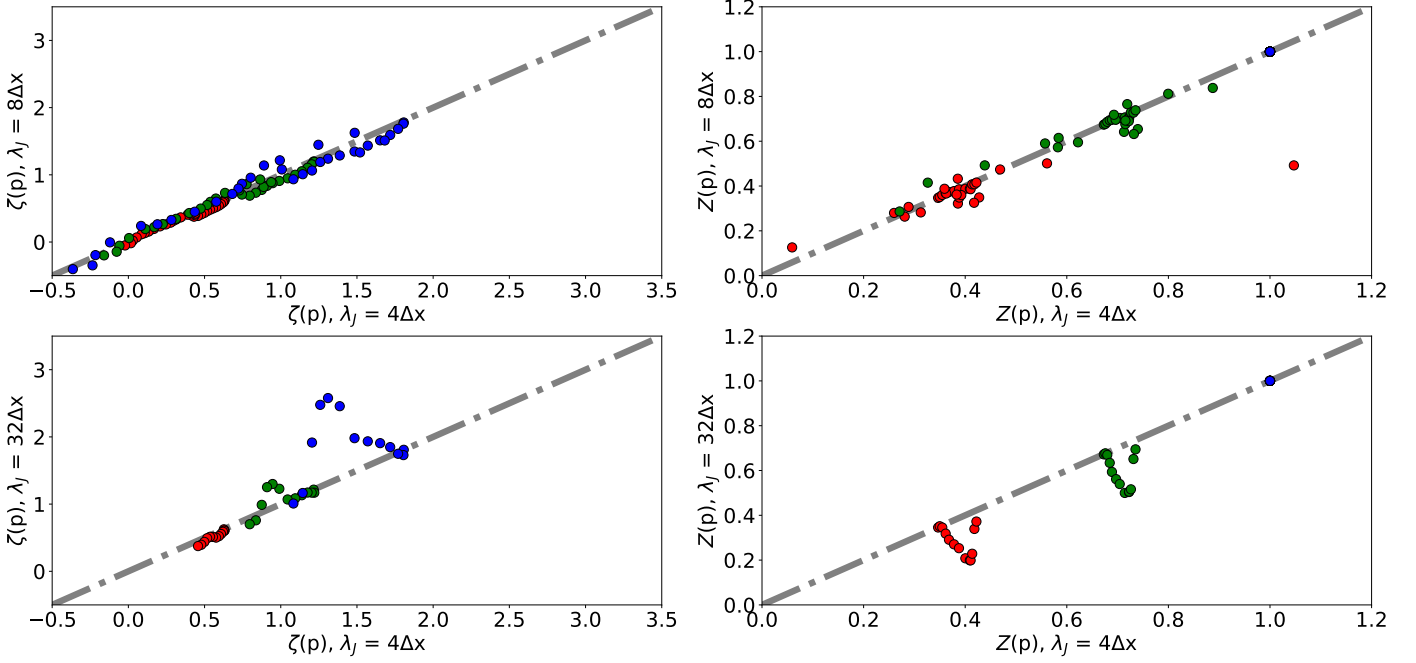
Figure 5: Comparison of VSF scaling exponents, ζ (*left*), and self-similarity parameters, Z (*right*), depending on the Jeans refinement of the simulation runs the data are based on. **Orders shown are** $p = 1$ (**red**), **2** (**green**), **and 3** (**blue**). The abscissas give values from $\lambda_J = 4\Delta x$, while the ordinates give values from $\lambda_J = 8\Delta x$ (*top*) and $\lambda_J = 32\Delta x$ (*bottom*). All data points refer to the M3 cloud and represent **different lags in** the same time step in the respective simulations.

icant effect. However, as the clouds evolve the differences increase: the non-weighted VSFs never drop below 0.5. This is because the non-weighted VSF treats all cells equally, no matter whether the particular cell represents a dense element of the cloud centre or a diffuse element of the cloud's edge, while the weighted VSF gives more weight to the matter within the **small-scale, dense, collapsing regions. The kinetic energy is dominated by these regions. Thus, neglecting density weighting decouples the VSF from the kinetic energy distribution. This is particularly important at late times when small-scale collapse dominates.**

Nevertheless, Fig. 3(d) illustrates that these differences **do not prevent extended self-similarity from holding. Regardless of whether density-weighting is included, the values of** Z **remain similar, with similar responses to external driving, except for the features created when** $\zeta(3)$ **passes through zero in the density-weighted VSFs.** This observation is true for all Jeans refinement levels, as Fig. 4 demonstrates.

We conclude that deriving the VSF from smooth density distributions without considering density-weighting does not affect the behaviour of ζ and Z, as long as the turbulence is dominated by large scale **flows, but** it has a significant effect on the measurements when the small scales become dominant. The latter is particularly important as this finding has a directly impact on the conclusions drawn based on the scales and mechanisms that drive the turbulence based on the measured ζ. Not only does ζ become insensitive to the influence of gravitational contraction with time, the non-weighted VSFs also do not reflect when the majority of kinetic energy has been transferred to small scales.

4.4. Jeans Length Refinement

In Fig. 5 we see that the choice of refinement level does not have to have a significant influence on the measurements and evolu-

tion of both ζ and Z. $\lambda_J = 4\Delta x$ and $\lambda_J = 8\Delta x$ are in **good agreement with each other.** This means that, although refining Jeans lengths with 4 cells misses about 13% of kinetic energy, the effect on the structure and behaviour of the turbulence is rather small and not traced by the VSF analysis.

However, Fig. 5 shows that the agreement is **rather poorer** with $\lambda_J = 32\Delta x$, as the latter differs more from $\lambda_J = 4\Delta x$ the higher the order of the VSF is. Following the explanations in Sect. 3.6, the behaviour of ζ and Z in the $\lambda_J = 32\Delta x$ runs corresponds to the reaction of the cloud's gas to a shock wave running through the cloud; caused by a supernova that exploded before $t = 0$ Myr. Indeed one sees a SN at a distance of 172 pc at $t = -1.11$ Myr. Due to the distance the SN is too weak to effectively compress the gas within M3 and cause a shock. This is why it was not detected in the less refined samples. However, the SN explodes far below the mid-plane of the simulated disk galaxy, in a region without dense gas, so **the blast wave remains strong** as it propagates through the ISM. By the time the blast arrives at cloud M3, it is still energetic enough to drive strong winds, with velocities above 300 km s^{-1}, at the closer edge of the cloud. This causes an increase of VSFs at longer lag scales and the increase of ζ, as well as the drop in Z. **We conclude that improving the resolution resolves details that can affect the VSF, but that the overall behavior is already determined by our moderate resolution simulations.**

4.5. Comparison to Observational Data

[completely new]

5. **Summary & Conclusions**

In this paper, we analyse the turbulent structures of molecular clouds that have formed within three-dimensional adaptive

| Reference	Target Object(s)	p	ζ	Z
Heyer & Brunt (2007)	^{12}CO J = 1-0	1	0.49 ± 0.15	0.49 ± 0.15
Heyer & Dame (2015)	30 MCs	1	0.24 ± 0.00	0.24 ± 0.00
	Taurus	1	0.26 ± 0.00	0.26 ± 0.00
Miesch & Bally (1994)	^{13}CO J = 1-0	1	0.43 ± 0.15	0.43 ± 0.15
		2	0.86 ± 0.30	0.86 ± 0.30
Padoan et al. (2003)	Perseus	1	0.50 ± 0.00	0.42 ± 0.00
		2	0.83 ± 0.00	0.72 ± 0.00
		3	1.18 ± 0.00	1.00 ± 0.00
	Taurus	1	0.46 ± 0.00	0.42 ± 0.00
		2	0.77 ± 0.00	0.72 ± 0.00
		3	1.10 ± 0.00	1.00 ± 0.00
Padoan et al. (2006)	Perseus	2	0.80 ± 0.10	0.80 ± 0.10
Roman-Duval et al. (2011)	^{13}CO J = 1-0	1	0.50 ± 0.30	0.50 ± 0.30
Zernickel (2015)	NGC 6334	1	0.38 ± 0.00	0.38 ± 0.00
		2	0.76 ± 0.01	0.76 ± 0.01
	NGC 6334	1	0.48 ± 0.01	0.48 ± 0.01
	($\ell \leq 4$ pc)	2	0.79 ± 0.01	0.79 ± 0.01

Table 1: Summary of observed ζ and Z in the literature.
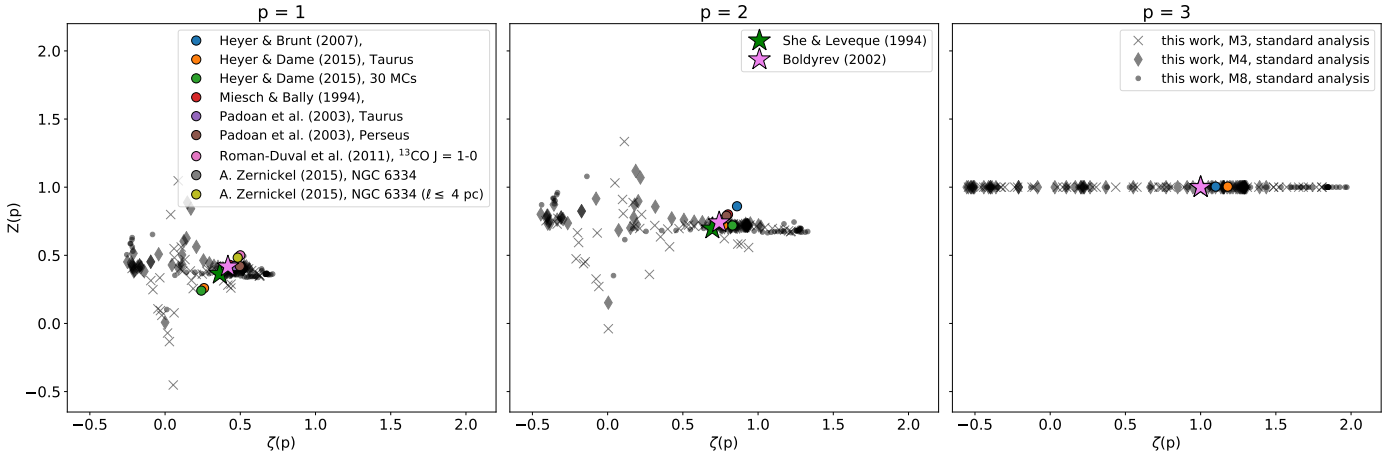
Figure 6: Summary of measurements of ζ (*abscissas*) and Z (*ordinates*) for orders $p = 1$–3 (from *left* to *right*) in this study and in the literature. The grey markers represent the values as presented in Sect. 3.2, while the coloured star markers illustrate the predictions by She & Lévêque (1994) and Boldyrev (2002). The coloured, circular marker summarise values found in the literature (see legend for precise references).

mesh FLASH simulations of the self-gravitating, magnetised, SN-driven ISM by Ibáñez-Mejía et al. (2016). The main results are as follows.

- The scaling of velocity structure functions (VSFs) is sensitive to both internal (gravitational contraction) and external (SN shocks, winds) driving sources of turbulence. Applied on simulated data, the time evolution of the scaling exponent, ζ, can reveal which driving mechanism dominates the turbulence of an entire molecular cloud. The self-similarity parameter, Z, though, is not directly sensitive to gravitational contraction. Yet, it can be used as observational tracer **for recent interactions with** SNe and winds.
- As long as the molecular cloud is not affected by a shock, Z is in good agreement with predicted values for supersonic flows. This makes it a fine probe for the properties of dominant turbulent modes, such as the geometry, and their evolution in the context with the evolution of the cloud.
- We test the influence of Jeans refinement on the VSFs. We find that the absolute amount of kinetic energy does not influence the evolution of ζ and Z, as long as the power spec-

trum is properly resembled, or similarly resembled by the compared samples.
- We see that the behaviour of the VSFs can be tracked with similar results based on 3D (i.e., from simulated data) and 1D (i.e., from observational data) velocity information, as long as there is no dominating flow driving the gas into a direction perpendicular to the line of sight. In the general case of a fully developed turbulent field, both ζ and Z evolve similarly in both scenarios, even though the actual values might not be in good agreement.
- We test the influence of introducing a density threshold on the VSFs. We see both quantitative and qualitative differences. The VSFs that based on the unfiltered data are much steeper than the cloud-only VSFs and do not reflect any interaction with any of the driving sources, including SN shocks. The measured Z values are constant in time and and for all clouds. This means that the turbulence we examine in this sub-project reflects the ISM in our entire galactic-scale simulations. The values of Z are slightly below the value predicted for a filamentary flow by She & Lévêque (1994). We conclude that the turbulence in the modelled ISM consists of vortices that are similar to filamentary flows, yet with a ra-

tio of average length scale of the two moments being more equal to unity than in the filamentary case.

– We investigate the influence of defining the VSF with and without taking density weighting into account. We see that the qualitative behaviour is traced by both approaches. Yet, the scaling of the non-weighted VSF is always positive and evolve flatter than they do for the density-weighted VSF. This means that non-weighted VSFs that are based on smoothed density distributions are biased against large scale motions and may not reveal the entire distribution of turbulent power within a molecular cloud.

Our analysis shows that VSFs are fine tools for examining the driving source of turbulence within molecular clouds. Therefore, we recommend its usage in future studies of molecular clouds. However, studies that utilise VSFs need to precisely review the assumptions and parameters they imply in their analysis as those can have a significant influence on the out-coming results.

For the simulated clouds, the VSFs illustrate that gravitational contraction dominates the evolution of the clouds, with short periods within which SN shock waves accelerate the turbulent powers on all scales. However, it requires further studies to verify this to be the common fragment formation scenario. In particular, a higher Jeans length refinement is needed to resolve the velocity structures on scales of individual grid cells (0.1 pc in this case) better. This is crucial for following the local behaviour of the gas as neither the average behaviour of the filaments nor the dominant turbulence driving source of the entire molecular clouds mirror the underling flow patterns of the gas that is related to fragmentation and the formation of future star formation activity.

References

Ballesteros-Paredes, J., Hartmann, L. W., Vázquez-Semadeni, E., Heitsch, F., & Zamora-Avilés, M. A. 2011a, Monthly Notices Roy. Astron. Soc. , 411, 65

Ballesteros-Paredes, J., Vázquez-Semadeni, E., Gazol, A., et al. 2011b, Monthly Notices Roy. Astron. Soc. , 416, 1436

Banerjee, S. & Galtier, S. 2013, Phys. Rev. E., 87, 013019

Benzi, R., Biferale, L., Fisher, R., Lamb, D. Q., & Toschi, F. 2010, Journal of Fluid Mechanics, 653, 221

Benzi, R., Ciliberto, S., Tripiccione, R., et al. 1993, PhysRevE, 48, R29

Boldyrev, S. 2002, Astrophys. J. , 569, 841

Boneberg, D. M., Dale, J. E., Girichidis, P., & Ercolano, B. 2015, Monthly Notices Roy. Astron. Soc. , 447, 1341

Brunt, C. M. & Heyer, M. H. 2013, Monthly Notices Roy. Astron. Soc. , 433, 117

Brunt, C. M., Heyer, M. H., & Mac Low, M.-M. 2009, Astron. Astrophys. , 504, 883

Burkhart, B., Collins, D. C., & Lazarian, A. 2015, Astrophys. J. , 808, 48

Chira, R.-A., Kainulainen, J., Ibáñez-Mejía, J. C., Henning, T., & Mac Low, M.-M. 2018, Astron. Astrophys. , 610, A62

Dekel, A. & Krumholz, M. R. 2013, Monthly Notices Roy. Astron. Soc. , 432, 455

Fleck, Jr., R. C. 1980, Astrophys. J. , 242, 1019

Fryxell, B., Olson, K., Ricker, P., et al. 2000, Astrophys. J. Suppl., 131, 273

Galtier, S. & Banerjee, S. 2011, Physical Review Letters, 107, 134501

Gotoh, T., Fukayama, D., & Nakano, T. 2002, Physics of Fluids, 14, 1065

Hartmann, L., Ballesteros-Paredes, J., & Heitsch, F. 2012, Monthly Notices Roy. Astron. Soc. , 420, 1457

Heyer, M. & Dame, T. M. 2015, Ann. Rev. Astron. Astrophys. , 53, 583

Heyer, M. H. & Brunt, C. 2007, in IAU Symposium, Vol. 237, Triggered Star Formation in a Turbulent ISM, ed. B. G. Elmegreen & J. Palous, 9–16

Heyer, M. H. & Brunt, C. M. 2004, Astrophys. J. Lett. , 615, L45

Ibáñez-Mejía, J. C., Mac Low, M.-M., Klessen, R. S., & Baczynski, C. 2016, Astrophys. J. , 824, 41

Ibáñez-Mejía, J. C., Mac Low, M.-M., Klessen, R. S., & Baczynski, C. 2017, Astrophys. J. , 850, 62

Kolmogorov, A. 1941, Akademiia Nauk SSSR Doklady, 30, 301

Krumholz, M. R., Bate, M. R., Arce, H. G., et al. 2014, Protostars and Planets VI, 243

Mac Low, M.-M. 2003, in Lecture Notes in Physics, Berlin Springer Verlag, Vol. 614, Turbulence and Magnetic Fields in Astrophysics, ed. E. Falgarone & T. Passot, 182–212

Mac Low, M.-M. & Klessen, R. S. 2004, Reviews of Modern Physics, 76, 125

McKee, C. F. & Zweibel, E. G. 1992, Astrophys. J. , 399, 551

Miesch, M. S. & Bally, J. 1994, Astrophys. J. , 429, 645

Miyamoto, Y., Nakai, N., & Kuno, N. 2014, PASJ, 66, 36

Padoan, P., Boldyrev, S., Langer, W., & Nordlund, Å. 2003, Astrophys. J. , 583, 308

Padoan, P., Juvela, M., Kritsuk, A., & Norman, M. L. 2006, Astrophys. J. Lett. , 653, L125

Padoan, P., Pan, L., Haugbølle, T., & Nordlund, Å. 2016, Astrophys. J. , 822, 11

Roman-Duval, J., Federrath, C., Brunt, C., et al. 2011, Astrophys. J. , 740, 120

Schmidt, W., Federrath, C., & Klessen, R. 2008, Physical Review Letters, 101, 194505

Seifried, D., Walch, S., Girichidis, P., et al. 2017, ArXiv e-prints

She, Z.-S. & Lévêque, E. 1994, Physical Review Letters, 72, 336

Tan, J. C., Shaske, S. N., & Van Loo, S. 2013, in IAU Symposium, Vol. 292, Molecular Gas, Dust, and Star Formation in Galaxies, ed. T. Wong & J. Ott, 19–28

Truelove, J. K., Klein, R. I., McKee, C. F., et al. 1998, Astrophys. J. , 495, 821

Turk, M. J., Oishi, J. S., Abel, T., & Bryan, G. L. 2012, Astrophys. J. , 745, 154

Zernickel, A. 2015, PhD thesis, I. Physikalisches Institut der Universität zu Köln, Zülpicher Straße 77, 50937, Köln, Germany ¡EMAIL¿zernickel@ph1.uni-koeln.de¡/EMAIL¿